Improved Turbine Vane Endwall Film Cooling by Using Sand-Dune-Inspired Design

ZHOU Wenwu[1,2], SHAO Hongyi[1,2], QENAWY Mohamed[1,2], PENG Di[1,2], HU Hui[3], LIU Yingzheng[1,2*]

1. Key Lab of Education Ministry for Power Machinery and Engineering, School of Mechanical Engineering, Shanghai Jiao Tong University, Shanghai 200240, China

2. Gas Turbine Research Institute, Shanghai Jiao Tong University, Shanghai 200240, China

3. Department of Aerospace Engineering, Iowa State University, Ames IA 50011, USA

Abstract: As continuous of the previous sand-dune-inspired design, the Barchan-Dune-Shaped Injection Compound (BDSIC)'s film cooling performance at the endwall region was further investigated both experimentally and numerically. While the public 777-shaped hole was served as a baseline, the BDSIC's endwall effectiveness was assessed at various blowing ratios. Experiments were performed in a single-passage transonic wind tunnel using pressure-sensitive paint (PSP) technique. Carbon dioxide was used as coolant with density ratio of DR=1.53. The purge slot's blowing ratio was fixed at M=0.3, but the coolant holes were adjusted within M= 0.5–2.0. The measured experimental results indicate that the film distribution at the endwall is strongly affected by the passage flow structures. The BDSIC holes demonstrate much higher film effectiveness than the 777-shaped holes for all blowing ratios, ~30% enhancement for regionally averaged effectiveness at M=1.0 and ~26% at M=2.0. As shown by the numerical results, the existence of BDSIC reduced the coolant penetration effect at a higher blowing ratio. Coolant was deflected and its momentum increased in the streamwise direction, therefore providing more robust film coverage over the endwall region. The anti-counter-rotating vortex pair induced by the BDSIC further stabilized the coolant film and increased the coolant spreading downstream.

1. Introduction

The rapid development of gas turbines demands for higher operating temperature of engine components for the increase of engine thermal efficiency [1–5]. This sets higher requirements for the cooling system, especially the nozzle guide vane (NGV) endwall region, which is located just downstream of the combustion and endures not only tremendous heat flux but also highly complex secondary flow [3]. Film cooling is one of the most important external cooling methods to protect the NGV endwall from extremely hot gas. Coolant is discharged from discrete holes and forms a film to protect the surface from the high-temperature gas flow. Improvements in the cooling scheme for the endwall region would ensure the structural integrity and

sustainable operation of the turbine, thus it is of great significance for the gas turbine community.

The challenge of turbine endwall film cooling lies in the highly complex external flow structures across the endwall, which tends to detach the coolant film and greatly deteriorate the cooling effectiveness. Langston et al. [6] experimentally studied the endwall flow structures and reported the incoming boundary layers separation, formatting the two legs of horseshoe vortex (HV) at the leading edge. The pressure side (PS) leg of HV merges to become part of the passage vortex (PV), while the suction side (SS) leg extends downstream to be the counter vortex (CV). These complex vortices intensively interact with the coolant film at the endwall region, which results in non-uniform coolant distribution and deteriorated cooling performance. This process was visualized clearly by Friedrichs et al. [7], who claimed that the cooled and uncooled region due to vortex interaction should be considered in the design phase. Kost and Nicklas [8] studied the strong interactions between horseshoe and passage vortex along with the coolant jet. Their results show that the endwall film cooling effectiveness decreased significantly near PS because of the existence of a passage vortex. Aside from the flow structures near the endwall, other studies have been done to explore the effect of cooling hole configurations and flow conditions on the endwall cooling effectiveness. Thole and Knost [9, 10] proposed a newly optimized cooling hole configuration and reported largely improved endwall cooling effectiveness. But they found that the leading edge and PS-endwall junction are difficult regions to cool due to the dead zone. Shiau et al. [11, 12] applied the pressure sensitive paint (PSP) to measure the film effectiveness and studied the injection angle and cooling hole distribution effect on the endwall cooling effectiveness. Chowdhury et al. [13] evaluated the mass flow ratio and coolant density ratio on the film cooling effectiveness of a typical endwall cooling design. Later chowdhury et al. [14] further studied the endwall film cooling with both slashface leakage and discrete holes. Müller et al. [15] comprehensively explored the influence of various slot geometry parameters such as widths, positions, injection angles, and flow conditions such as density ratio and blowing ratio effect on slot film cooling. The endwall film cooling is very complex that not only affected by the flow structures and cooling configurations, but also strongly influenced by the shape of cooling holes.

Shaped holes and innovative structures have been another focus for researchers to improve the endwall film cooling effectiveness. Barigozzi [16] measured the endwall film cooling with a fan-shaped hole and reported largely increased effectiveness over cylindrical holes. The influence of hole shape on film cooling was investigated by Colban and Thole [17, 18]. The results show that the shaped holes provide better film cooling performance and less total pressure loss than the circular holes. Also, Sundaram and Thole [19, 20] combined bump and trench with circular holes and successfully enhanced the endwall film cooling effectiveness. But an increased secondary loss was reported by Barigozzi [21] for trenched holes. Other proposed film cooling holes, such as Elliptical and Super-elliptical Holes [22], Combined Holes [23], Double Holes [24], Tree-like Holes [25], demonstrate improved film cooling performance, which are potential candidates for endwall film cooling applications. Recently, inspired by the unique flow structures induced by sand dune in the desert, Zhou and Hu [26, 27] presented the BDSR (Barchan-Dune Shaped Ramp) design, which showed ~15% enhancement in endwall cooling effectiveness compared with circular holes. Latterly, Zhou and Hu [28, 29] further optimized the BDSR to Barchan-Dune-Shaped Injection Compound (BDSIC), where the latter could not only alleviate the detrimental counter-rotating vortex pair (CRVP), but also ensure coolant discharged tangentially from hollowed dune shell. Compared with the circular hole, this novel BDSIC demonstrated an improvement of 30%–400% in film cooling effectiveness over a flat plate. Due to its promising performance, it is highly desired to further explore BDSIC application in the endwall region, where the dune can be used to reduce secondary flow and enhance endwall cooling.

In the present study, the influence of hole geometry (i.e., 777-shaped holes and BDSIC holes) on the film effectiveness was explored. CO_2 was selected as the coolant gas, which was separately injected from an upstream purge slot and a single row of holes. Endwall effectiveness at various blowing ratios (i.e., M=0.5, 1.0, 1.5, 2.0) was obtained for both configurations by applying PSP technique in a transonic wind tunnel. The experimental results were presented in terms of mean effectiveness contours, laterally-/area-averaged effectiveness plots. Additionally, numerical results with detailed flow structures on the endwall film cooling were shown to bring insight into the endwall cooling physics. This work is intended to improve the endwall film cooling performance by using BDSIC, which can be fabricated with the turbine as an integral component when additive manufacturing for hot section components is feasible in the future.

2. Experimental Setup

2.1 Test model and flow conditions

The experiments were conducted in a single-passage transonic wind tunnel in the School of Mechanical

Engineering, Shanghai Jiao Tong University. The layout of the test facility referred to the design proposed by Buck and Prakash [30] and further extended by Kodzwa et al. [31, 32], in which a single passage formed by two curved blade surfaces, while the periodic flow condition was guaranteed by bleeding gas from the upstream ports at the blade leading edge. The wind tunnel test system and PSP experimental measurements is shown in Fig. 1. Detailed procedures for single-passage wind tunnel design can be found in Ref. [33].

Mainstream flow inside the test vane was driven by a 132 kW screw compressor upstream. Water, oil, and dust particles inside the flow are removed when the flow passes through a series of filters (SMC-AF900, SMC-AMD850) downstream of the compressor. Two pressure regulating valves (SMC-AR925) installed in the flow path were used to reduce and stabilize the total pressure. A major flow control valve was installed downstream to control the flow rate of mainstream flow, setting the proper flow condition desired for this study. The mainstream flow then entered a settling chamber with aluminum honeycombs and meshes installed inside

to reorganize the flow fed by the pipelines before it enters the test section. The velocity inside the test section was monitored by a five-hole probe. The stagnation temperature of mainstream flow and coolant was separately monitored by a series of K-type thermocouples installed inside each's plenum. During the testing, the incoming velocity was maintained at 52±0.5 m/s, and the corresponding Mach number at the exit was Ma=0.85. The turbulence intensity was estimated to be ~2.1% according to the hot-wire anemometer. The incoming boundary layer was experimentally checked to be fully developed turbulence with a thickness of $\delta_{99} \approx 3.1D$ in the test section.

The test section, constructed by UV-curable resin by a digital light processing (DLP) 3D Printer (layer thickness 50 μm), was installed downstream of the plenum. The interior surface was carefully polished to guarantee its surface quality by using 1000-grit sandpaper. The view side of the endwall was made of Plexiglas to allow for optical access to the UV-LED lamp and high-speed camera. In terms of the blade geometry, the wind tunnel employed the high-pressure turbine vane geometry,
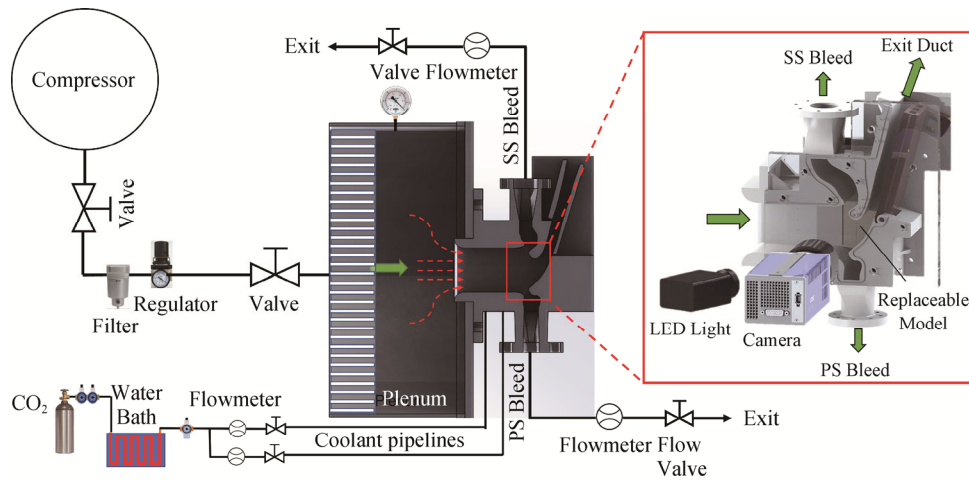
(a) Schematic of the single-passage model and experimenetal setup
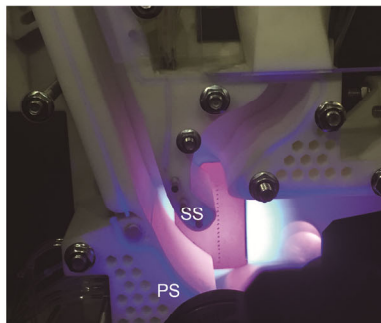
(b) Endwall cooling with LED on
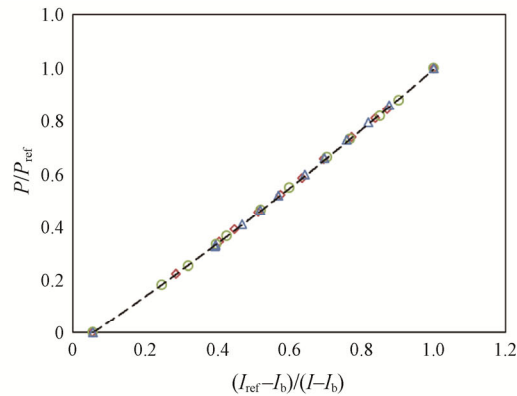
(c) PSP calibration curve

Fig. 1   The single-passage test system and schematic setup for the PSP experiments

which was proposed by the von Karman Institute (VKI) [34]. The blade chord length was C=67.6 mm and the blade height was H=75 mm. Blade pitch to chord ratio was P/C=0.85. Two bleed ports were positioned at the upstream of the blade leading edge to maintain proper flow condition inside the single passage. The volumetric flow rate of two bleed ports was separately monitored and carefully controlled by the flow meters (SMC-PF3A706H and SMC-PF3A703H) and valves installed in the flow path. The flow rate for the two bleed ports was pre-determined by CFD results and testing was done before the film cooling experiment to examine the isentropic Mach number distribution at mid-span through static pressure probes. Note that only ~7% of the air supplied discharged from the two bleed ports altogether, and the rest 93% air flows through the main passage, which makes the single-passage cascade design an energy-efficient choice compared with the multiple-passage cascade design. Table 1 summarizes the vane's geometrical dimensions and the single passage flow conditions.

Table 1   Geometric information and mainstream conditions

Scaling factor	1
Hole diameter, D	1.0 mm
Hole entry length, L/D	9
Hole injection angle	35°
Holes spacing, P/D	3
Slot width, W/D	1.5
Slot entry length, L/D	5
Slot injection angle	90°
Chord length, C	67.6 mm
Axial chord, C_{ax}	51.8 mm
Vane height	75 mm
Pitch/chord, P/C	0.85
Stagger angle	55.0°
Inlet angle	0°
Inlet velocity, U_∞	52 m/s
Exit Mach number, Ma	0.84

Fig. 2 shows the geometric configurations of the 777-shaped and BDSIC endwall test models. Both models were constructed through UV-curable resin layer-by-layer with a resolution of 50 μm. The endwall surface was carefully polished with 1000-grit sandpaper and then thoroughly cleaned to remove any dust or stain on it. The test model consists of an upstream purge slot (i.e., to simulate the gap leakage flow within engine components) and a downstream single row of holes. The region of interest on the endwall surface extends from the slot to approximately 40% of x/C downstream of the

coolant holes. The slot is located at 20D upstream of the cooling holes, which has W/D=1.5 and an injection angle of 90°. A total of 22 cooling holes (diameter D=1 mm) are evenly distributed across the endwall passage with a pitch ratio of P/D=3, locating 4D upstream of the turbine vane's LE. The inlets for both configurations are cylindrical and injection angle of α=35°, but their exit shapes are different. For the 777-shaped hole, the entry length is L/D=4.8 and the exit part has a diffusion angle of 7° in bilateral and streamwise directions [35]. For the BDSIC hole, its shape was generated from a topographic map of an idealized Barchan dune [28]. It has a height of 0.6D and width of 2.85D, featuring a hollowed shape that is positioned right above the circular tube. The coolant jet is first guided to impinge on the internal surface and then discharges into the mainstream flow tangentially. The BDSIC design can be treated as an upgraded version of BDSR presented in the previous work [26, 27], where the former is a solid ramp, but the present study is a hollowed dune.

In the present study, the coolant was supplied from a pressurized CO_2 gas cylinder (99.99% purity). The density ratio of coolant over mainstream ($DR=\rho_c/\rho_\infty$) is 1.53. Before entering the cooling holes, the coolant stream passes through a heat exchanger which is a long copper tube merged in the constant-temperature water basin. In this way, it can ensure the coolant and mainstream maintaining same temperature before exiting the coolant slot and holes. Two plenums separately fed the coolant to the slot and the coolant holes. The coolant mass flow rates were separately monitored and controlled by two flow meters (OMEGA FMA-1610A) and valves located in the flow path, as shown in Fig. 1, to realize the designated nominal blowing ratio. Uncertainties of the flow rate reading were less than 1% during the experiment. The blowing ratio of the purge slot was fixed at M=0.3 to simulate the small gap leakage flow within engine components [15], while for the coolant holes it varied between M=0.5, 1.0, 1.5, 2.0.

As the study uses a single-passage wind tunnel design, the pressure and isentropic Mach number were compared with multi-passage design VKI MUR43 [34] before the experiments. In Eq. (1) isentropic Mach number is defined to describe the aerodynamic loading on the blade surface, where P represents the measured static pressure at mid-span of blade surface; P_0 represents the mainstream flow's stagnation pressure, and γ is the specific heat ratio.

$$Ma = \sqrt{\frac{2}{\gamma-1}\left[\left(\frac{P_0}{P}\right)^{\frac{\gamma-1}{\gamma}}-1\right]} \quad (1)$$

A total of 27 pressure taps (i.e., diameter of 0.7 mm), with 8 taps on PS and 19 taps on SS are arranged for this measurement. The pressure taps are perpendicular to the
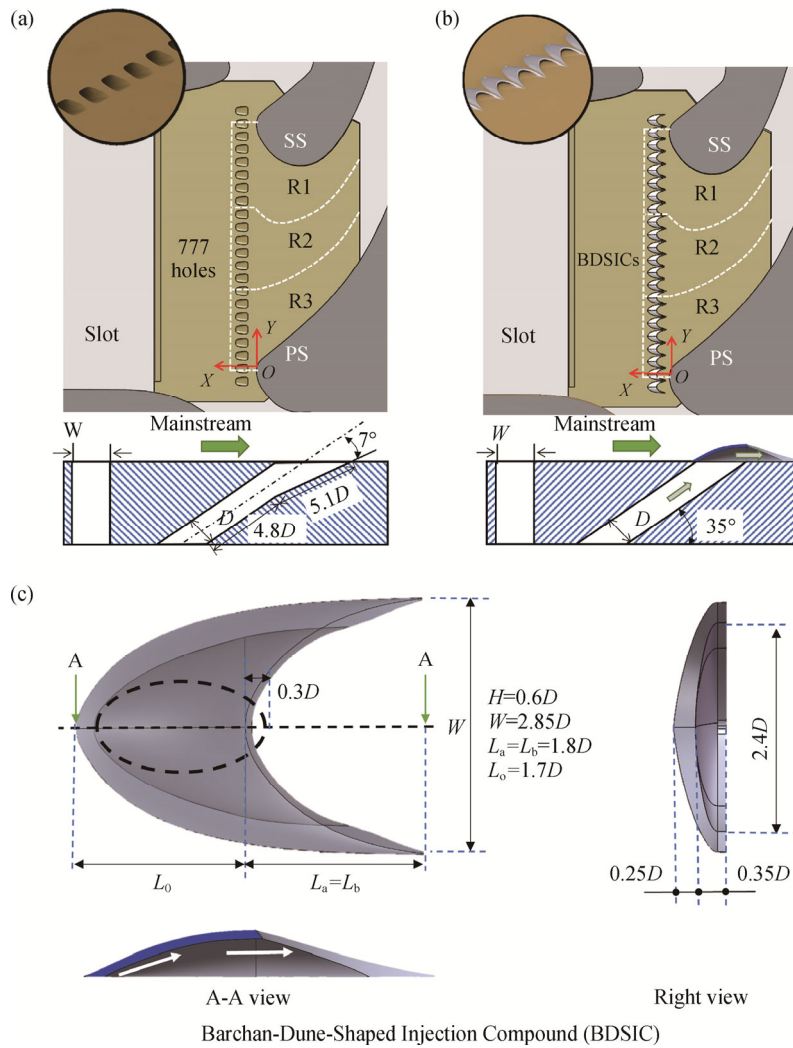
Fig. 2 The geometric configurations of (a) 777-shaped hole, (b) BDSIC models, and (c) detail geometry of the BDSIC, where *D* is hole's diameter

blade surface and connected to the pressure transducer (DAQ-DBX-32C). It was found that the present study is consistent with the archived multi-passage wind tunnel testing [33].

2.2 Experimental method

Adiabatic effectiveness is a non-dimensional number which is defined below in Eq. (2), where T_r refers to the recovery temperature, T_{aw} refers to the temperature of adiabatic wall, and T_{tc} is the coolant total temperature.

$$\eta = \frac{T_r - T_{aw}}{T_r - T_{tc}} \quad (2)$$

In contrast to the non-isothermal methods, such as infrared techniques, the PSP technique measured the adiabatic wall temperature T_{aw} based on mass transfer analogy [36, 37]. The zero temperature difference allows researchers to eliminate heat conduction errors during testing. When excited by the ultraviolet (UV) light, shown in Fig. 1, the PSP luminescent molecules will emit

photoluminescence where intensity is related to local oxygen partial pressure over the test surface. By discharging a foreign gas from coolant holes, the local oxygen partial pressure varies in a way analogous to the heat transfer process, resulting in a contour with different luminescent intensities over the surface. According to mass transfer analogy, the adiabatic cooling effectiveness is thus expressed as a function of local oxygen concentration (Eq. (3) [38]), where *MW* is the coolant's weight ratio over mainstream gas:

$$\eta = \frac{T_\infty - T_{aw}}{T_\infty - T_c} \approx \frac{C_\infty - C_w}{C_\infty - C_c} = 1 - \frac{1}{1 + \left(\dfrac{p_{O_2,air}}{p_{O_2,fg}} - 1 \right) MW} \quad (3)$$

The endwall model was evenly coated with an in-house prepared PSP which consists of luminescent molecules (Pt-FPPP in this case) and a gas-permeable polymeric ceramic (PC) binder. The quantitative relationship of oxygen partial pressure and the

luminescent intensity was determined by PSP calibration process, where the calibration curve is shown in Fig. 1(c). A UV-LED lamp (Prizmatix UHPT-LED-385, wavelength 385 nm) was the excitation source. The intensity ratio variation for the LED lamp was tested to be less than 0.5%. The PSP photoluminescence was captured by a high-speed CMOS camera (PCO-HS4), where the frame rate was 10 Hz and exposure time was 5 ms, separately. A bandpass filter with a wavelength of (650±25) nm was equipped in front of the lens to filter the signal from the excitation light and background noise. The intensity value of the camera is examined to show a linear response with exposure time.

For the PSP post-processing, a 6×6 pixels interrogation window was used to reduce the measurement uncertainty (50% overlap). The in-house MATLAB code was utilized to calculate the adiabatic effectiveness contour (400 snapshots). Referring to Johnson and Hu's work [39], the relative uncertainty was determined to be ~4% for mean effectiveness of η=0.5 and 11% for mean value of η=0.2 after considering the temperature variations over the test surface. The measurement uncertainty is related to the temperature variation over the surface, quality of the recorded frames, flow conditions, and PSP calibration processes.

3. Results and Discussion

3.1 Adiabatic effectiveness and standard deviation distributions

Figs. 3 and 4 show the measured adiabatic effectiveness distributions between the 777-shaped and BDSIC configurations with slot blowing ratio fixed at M=0.3 and coolant hole at M=0.5 and 1.0. The orange contour shows the high film effectiveness region while the white indicates the low-value region. The time-averaged film cooling effectiveness is obtained by taking the mean of instantaneous effectiveness (i.e., $\eta(x, z, t)$, shown in Eq. (4), where the non-dimensionalized streamwise and spanwise coordinates are represented by x and z coordinates,

$$\bar{\eta}(x,z) = \frac{1}{t}\int_0^t \eta(x,z,t)\,\mathrm{d}t \qquad (4)$$

As shown in Figs. 3 and 4, the measured contours show asymmetrical film distributions over the endwall that the coolant accumulates towards the blade SS, rendering higher effectiveness near the SS region, which matches with the achieved results [10]. The upstream slot exhibits almost the same signatures for all cases since the blowing ratio is constant. Its coolant initially spreads widely spanwise but quickly converges along streamwise before interacting with downstream coolant flow.

As for the coolant discharged from the holes shown in Fig. 3(a), its dispersion varies largely over the endwall
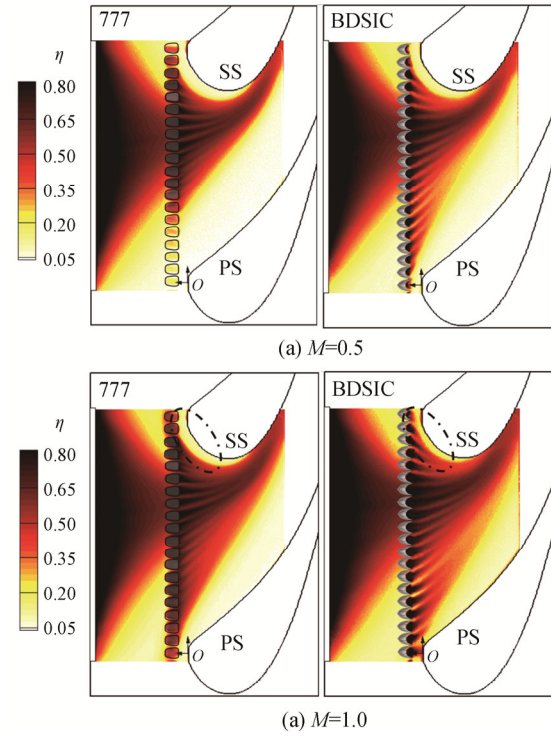
Fig. 3 Measured effectiveness distributions of the 777-shaped holes and BDSIC holes at M=0.5 and 1.0

region from PS to SS caused by the pressure gradient spanwise on the passage endwall. Almost no coolant was discharged from the 777-shaped holes near the PS region, while the BDSIC demonstrates much better coolant coverage. Compared with the 777 hole, the BDSIC presents a much wider and more evenly distributed film. But for both hole configurations, the coolant is forced by the flow structures (i.e., passage vortex) to move from PS to SS, therefore the downstream region near-PS is relatively uncooled. Carefully examining the leading-edge region of SS endwall, rarely any coolant is observed at the endwall junction indicating that the horseshoe vortex sweeps the coolant into the mainstream flow.

Increasing to M=1.0, the 777-shaped holes present a significantly increased coolant coverage compared with the M=0.5 case. The aforementioned converging coolant trace becomes much wider and more uniform. Though a similar trend is observed for the BDSIC, its cooling effectiveness is much higher near the PS and SS regions. The BDSIC has exhibited a much higher tangential momentum [28] that can resist the crossflow deflection caused by the passage vortex, while for 777-shaped holes the coolant is diverted immediately after leaving the holes. The BDSIC can thus provide much better coolant coverage than the shaped hole over the endwall region. Not only that, but the ejected coolant of BDSIC also spreads closer to the leading-edge junction of SS, where is hard to cool region [10].

Further increasing to M=1.5 and 2.0, no significant blow-off of coolant stream is observed for both 777-shaped and BDSIC holes. The film effectiveness of 777 shaped hole locally increased and coolant shows much better coverage than the M=0.5 and 1.0, especially for the near the PS and SS of blade. The increased momentum of coolant jets can overcome the negative pressure within the passage. However, the BDSIC holes demonstrate an almost fully cooled endwall region, except the downstream locations. Regions showing significant improvement in film effectiveness, such as the endwall region near SS leading-edge, middle, and near the PS, are observed for BDSIC configuration. Due to the favorable effect of hollow dune, the coolant discharged from BDSIC stays closer to the wall and is less influenced by the complex secondary flows. It is worth noticing that the blade-endwall conjunction near the SS leading-edge is well covered for the BDSIC at M=1.5 and 2.0, showing greatly enhanced protection for the relatively hard-to-cool region. Therefore, the BDSIC demonstrates great potential for endwall film cooling.

Fig. 5 shows the comparisons of standard deviations (SDs) between the 777-shaped and BDSIC holes at various blowing ratios. The general patterns of SD distributions for both configurations are similar,
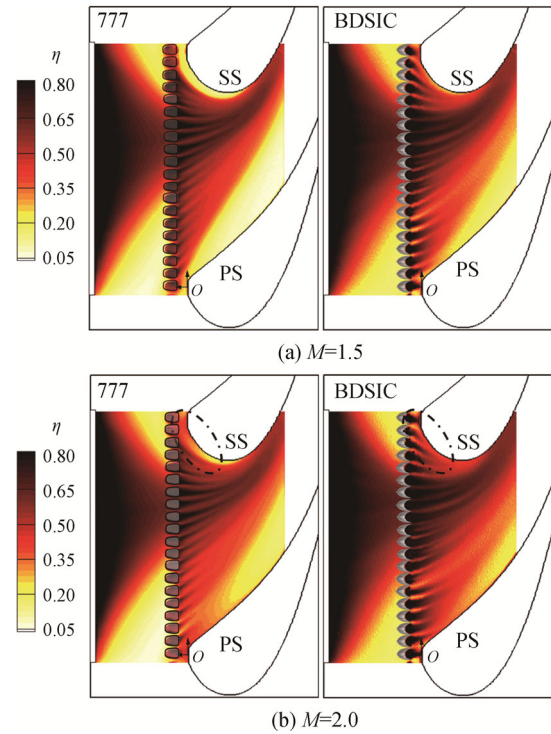

(a) M=1.5

(b) M=2.0

Fig. 4 Measured effectiveness distributions of the 777-shaped holes and BDSIC holes at M=1.5 and 2.0
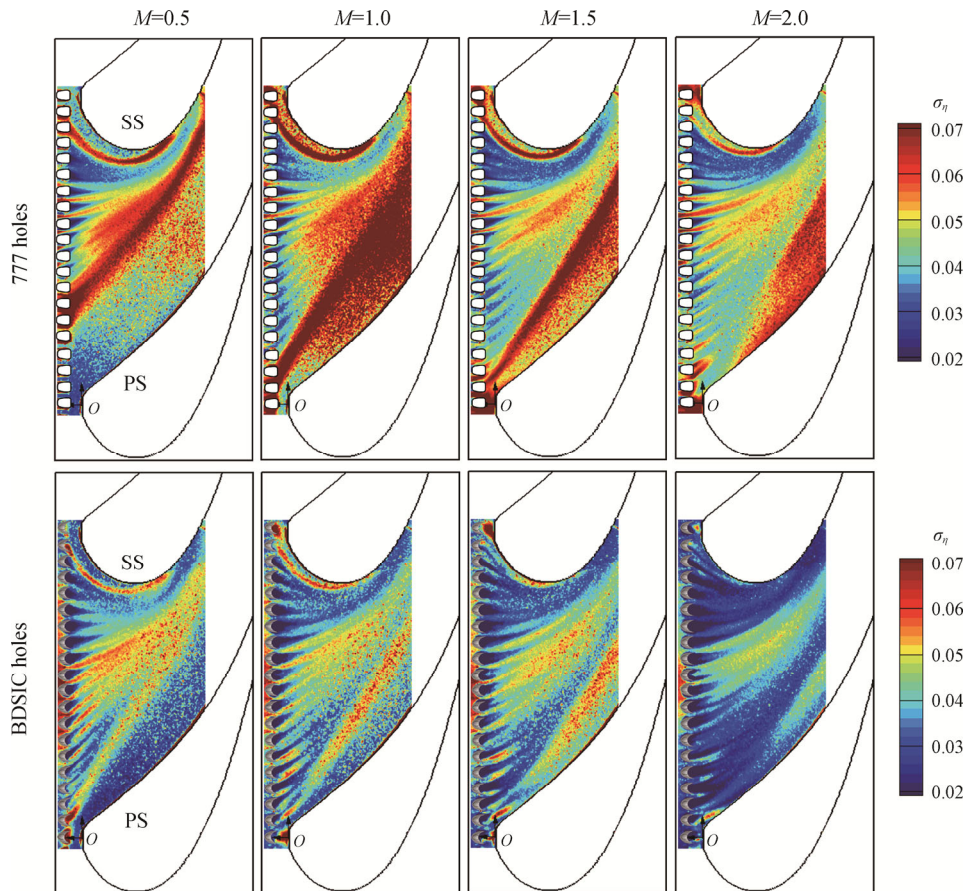

Fig. 5 Comparisons of standard-deviation distributions between the 777 and BDSIC at different blowing ratios

demonstrating relatively low SDs in the near-SS region but much higher traces within the coolant-mainstream interfaces (one near the leading-edge of SS, another near the middle or PS). Because of the intensive interactions of coolant and flow structures, the effectiveness variations along the coolant interfaces are much greater than others. As the M increased from 0.5 to 2.0, the SDs are found to decreased gradually, showing more stable film coverage. Though the general SD contours are similar, the absolute fluctuations of BDSIC are greatly lower compared with the 777 holes. Because of the existence of hollowed shell, the coolant would discharge tangentially into the mainstream and interacts less with the incoming flow, resulting in much stronger momentum and more stable coolant coverage.

3.2 Laterally averaged effectiveness distribution

To further assess the performance of film cooling quantitatively, lateral results were extracted spanwisely from the measured effectiveness contours. They are averaged over the blade pitch, and the zero point of axial location is set at the leading edge. Fig. 6 compares the results of two different configurations at various blowing ratios, where the previous endwall BDSR's results [26] were also shown here for comparisons. Both the 777 and BDSIC holes exhibit better performance than the previous BDSR. As for the 777-shaped holes and BDSIC holes, the lateral effectiveness rises with an increase in M. The general pattern of laterally averaged effectiveness is a falling pattern, where the effectiveness is decreasing in streamwise direction. Though the 777-shaped hole shows high effectiveness, the BDSIC greatly outperforms the 777-shaped holes at all cases. Ranging from M=0.5 to 2.0, the discrepancy between them is found to become larger as the blowing ratio increase because of the complex flow structure along the passage channel. More specifically, a 20% increase is achieved at M=2.0 for the BDSIC comparing to the 777-shaped hole. The nature-inspired dune shape exhibits an increasing benefit to the film cooling effectiveness for increased M, which corresponds with the conclusions of previous dune studies [28, 29].

The measured endwall effectiveness is locally dependent due to the passage vortex, where the film
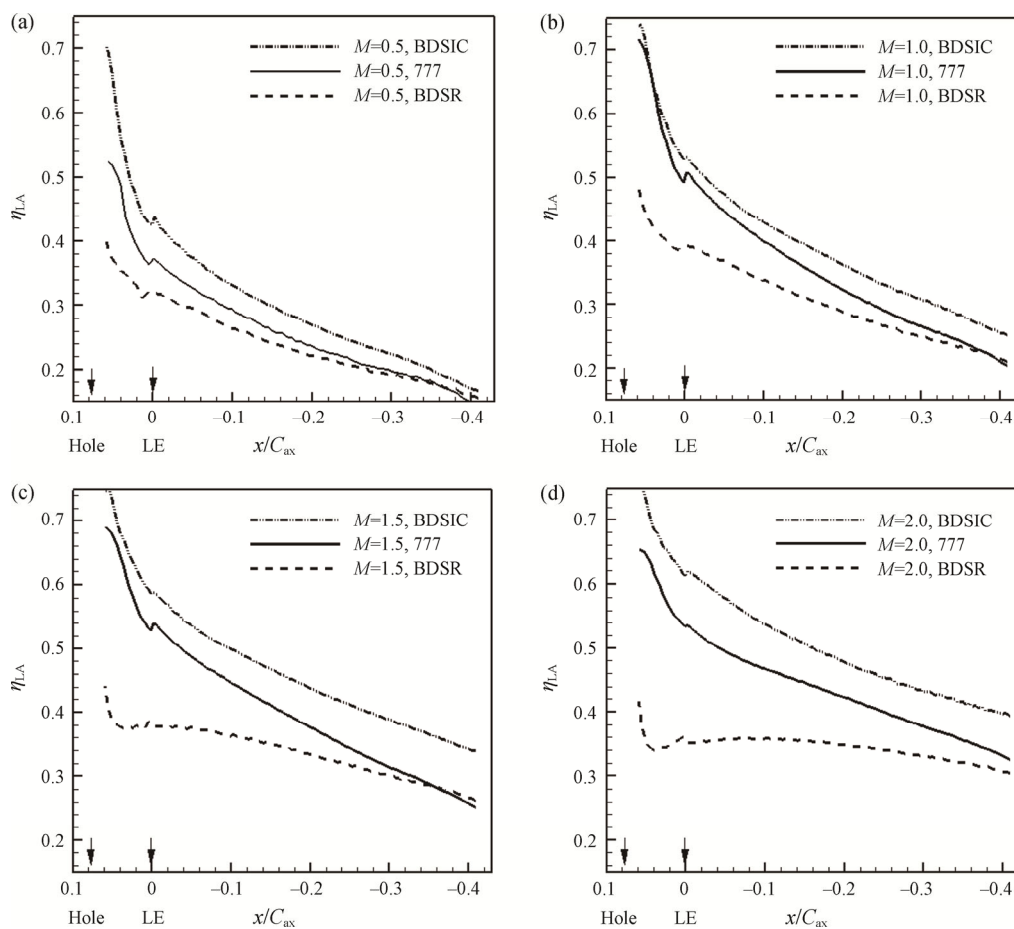
Fig. 6 Laterally-averaged effectiveness of the BDSIC, 777, and BDSR holes, where the BDSR's results were reproduced from Zhou et al. [25]

cooling contours show dramatically different phenomenon from PS to SS. To further investigate the regional behavior of endwall film cooling behavior, the measured effectiveness contours were examined separately as shown in Fig. 2. Referring to Knost and Thole's work [10], three separate regions are divided spanwisely as trisections of the single-passage channel,

and the laterally-averaged effectiveness is calculated respectively: R1 is defined as the endwall region located near the SS, and R2 represents the middle of the passage while R3 is the region near PS.

Fig. 7 shows the regionally laterally-averaged effectiveness of 777 shaped holes and BDSIC within Regions 1, 2, and 3. Generally, R1 has the highest
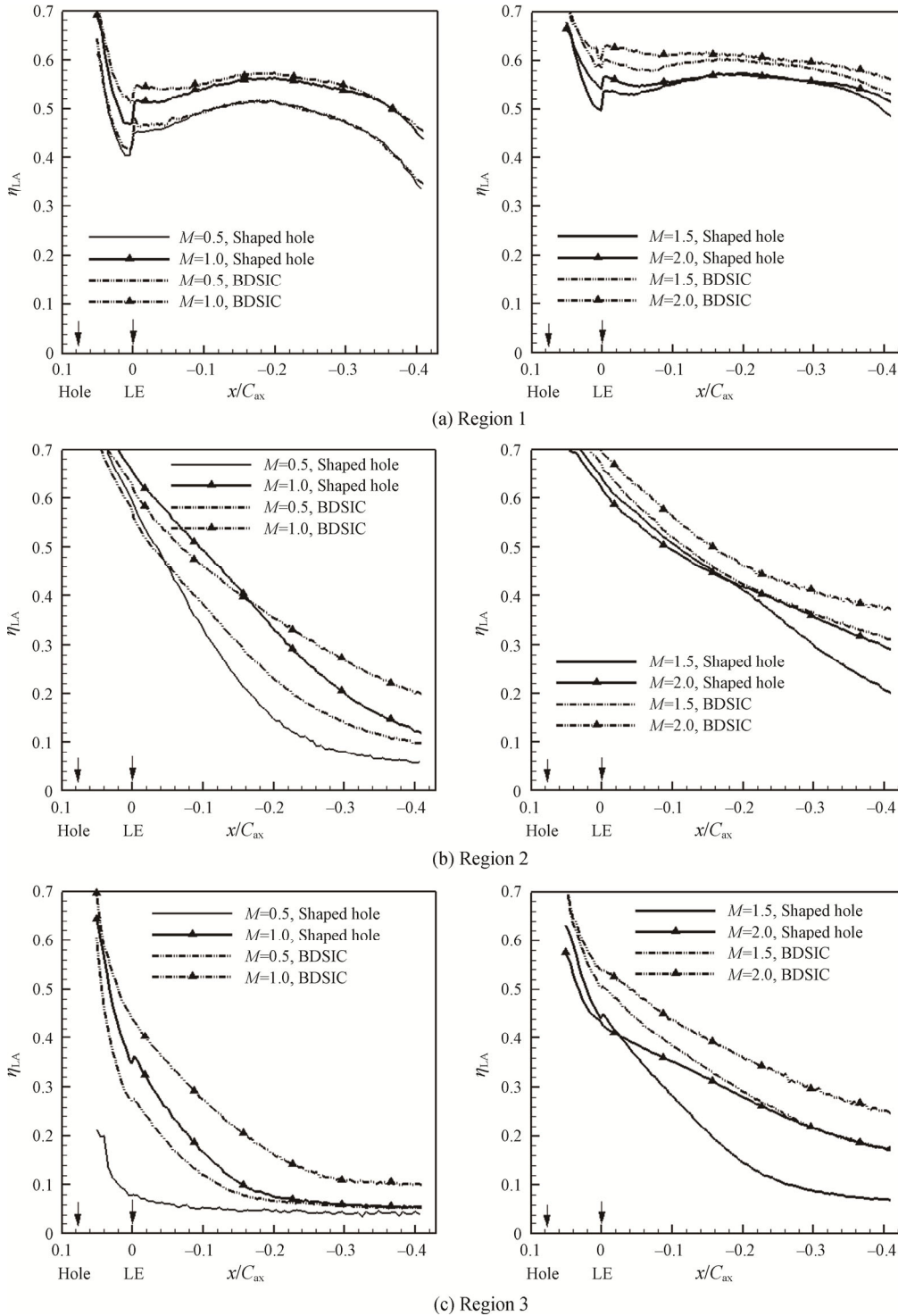

(a) Region 1

(b) Region 2

(c) Region 3

Fig. 7 Laterally-averaged effectiveness within Regions 1, 2, and 3

cooling effectiveness, following by R2, while R3 has the lowest values. Because of the pressure gradient across the channel, the jet stream would shift to the SS that accumulated in R1, resulting in the best film coverage. As shown in Fig. 7(a), both the 777-shaped holes and BDSIC show high film cooling effectiveness along the chord direction for R1. A weak dependence is observed for measured effectiveness as the M increased, only slightly increase in effectiveness as M adjusted within 0.5–2.0. This phenomenon indicates well coolant film coverage near the SS of endwall passage. Though the 777-shaped holes perform well, the BDSIC shows enhanced effectiveness at higher M, especially for M= 1.5, 2.0 (~11% enhancement at M=2.0).

In terms of R2 and R3, as the M increased, both hole configurations display a significant enhancement in film effectiveness, indicating enhanced coolant coverage over the endwall surface. In the region namely R2, the shaped hole shows higher effectiveness in the near-hole region, but the BDSIC surpasses it downstream at M=1.0 and 1.5. For higher blowing ratio of M=2.0, the BDSIC completely exceeds the shaped hole with an enhancement of 25% in lateral effectiveness. In addition, the shaped hole shows a faster effectiveness decline along the streamwise direction, while the BDSIC is much slower, indicating a more robust coolant ejected from the BDSIC compared with the baseline. As for the R3, the effectiveness of both configurations is much smaller than that of R1 and R2, manifesting insufficiently cooling near the PS. The lateral effectiveness of BDSIC is found to be greatly higher than the 777 shaped holes at all cases. More specifically, the BDSIC demonstrates more than 30% enhancement in comparison with the baseline at M= 1.5 and 2.0.

3.3 Area-averaged effectiveness distribution

To further evaluate the overall film cooling, the effectiveness is averaged within the passage area. For all cases, the area of interest is bounded by the PS and SS within the passage that starts from the slot and ends at 40%C_{ax}. R1 and R3 are presented to illustrate the effectiveness difference of near PS and SS, respectively.

Fig. 8 shows comparisons of the area-averaged effectiveness between the 777-shaped holes and BDSIC at various blowing ratios, where the BDSR's results [26] were presented for reference. Clearly for both configurations, the area-averaged profiles are higher than the previous BDSR. The effectiveness of both 777 and BDSIC is found to increase as the M increases. Their geometry features help alleviate the jet separation at higher M, leading to continuous enhancement of area-averaged effectiveness. But the BDSIC demonstrates a great advantage over the 777-shaped

holes in terms of endwall cooling. If averaged over the entire region, the BDSIC shows a 15% increase at M=0.5, 13%, and 14% increase at M=1.5 and 2.0 respectively. If averages the effectiveness regionally, it still reaches the same conclusion: for R1 near the SS of blade, the BDSIC holes show less advantage at M=0.5 and 1.0, however at M=1.5 and 2.0 the effectiveness raises 6% and 8% respectively. The most significant improvement happens in the endwall region near the PS (namely, R3). The area-averaged effectiveness when employing BDSIC holes showed as much as 150% and 26% enhancement over 777-shaped holes at M=0.5 and 2.0 respectively.
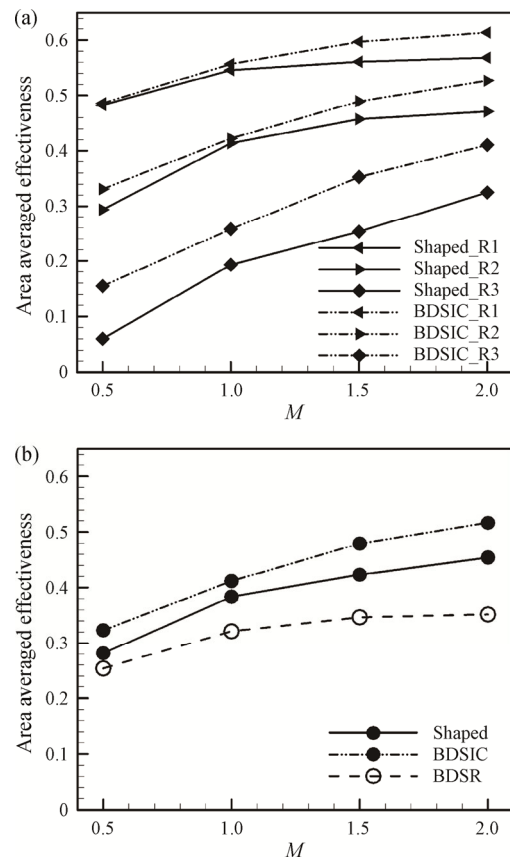
Fig. 8　The area-averaged effectiveness of the BDSIC and 777 shaped holes at various blowing ratios within R1, R2, and R3, where the BDSR's results were reproduced from Zhou et al. [25]

In general, the BDSIC is capable of increasing the cooling performance at the endwall region near the PS. As for the near the SS and middle of the passage, the BDSIC also shows better performance at higher blowing ratios. Therefore, the BDSIC exhibits promising potential for endwall cooling applications, while the hole distributions should be cautiously evaluated due to the strong relationship between its performance and the local flow features.

3.4 Numerical setting and validation

To reveal the underlying princples for endwall cooling, endwall film cooling simulations with 777-shaped holes and BDSIC holes are performed using ANSYS FLUENT 18. The geometry and corresponding mesh are presented in Fig. 9(a). Star CCM+ was used in this study to generate a high-quality unstructured polyhedral mesh. The near-wall meshes were composed of 20 prismatic layers and the first layer maintains $y^+<1$ to ensure the resolution of near-wall flow field. Refinements of meshes were made at the cooling geometries to increase the resolution. The mesh was proved to be independent with the variation of laterally-averaged effectiveness, less than $\Delta\eta=1\%$ at grid of 10 million cells.

The boundary conditions were set to be the same as the experimental conditions, including the incoming flow conditions. The pressure inlet for the mainstream is set at an absolute pressure of 1.44×10^5 Pascal, and a pressure outlet of 1×10^5 Pascal is applied to the flow exit. The exits of SS and PS bleed ports were set as pressure outlets with 1.421×10^5 Pascal and 1.418×10^5 Pascal, respectively. Symmetric plane was set at the mid-height of the blade to save computational resources. Total temperature of mainstream inlet is set at 450 K. The upstream slot and the cooling holes were velocity inlets with nominal blowing ratio $M=0.3$ and $M=1.5$, respectively. The coolant temperature was set to be 300 K and reached a density ratio of $DR=1.5$.

The steady-state RANS was conducted with a segregated solver and it utilized an implicit pressure correction. The working fluid was air and it was treated as an ideal gas. In terms of turbulence model, both the
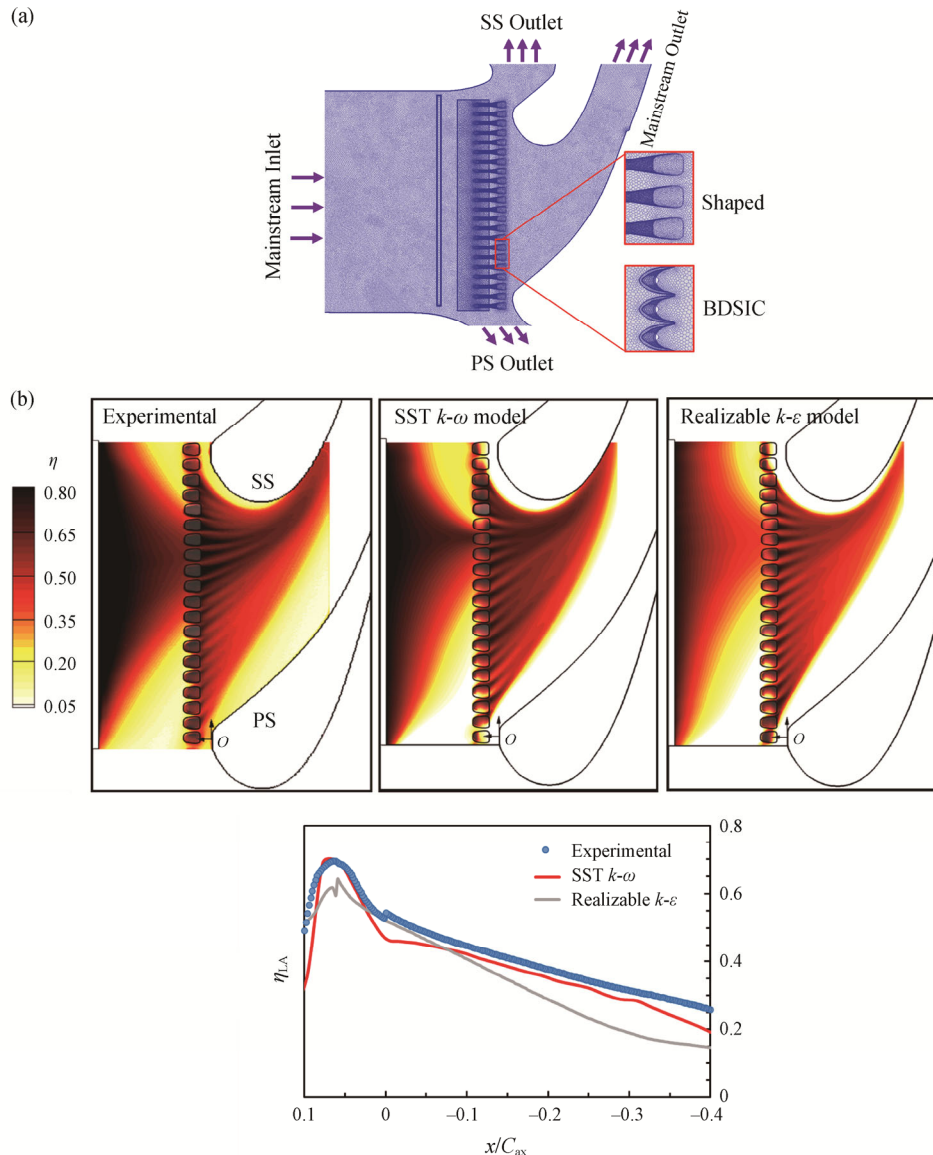
Fig. 9   Numerical setups of (a) mesh overveiw and boundary conditions, (b) comparison of numerical and measured film effectiveness with 777-shaped holes at $M=1.5$

shear stress transport (SST) k-ω model and Realizable k-ε model [40] were tested for this study side by side. Since the latter one underestimated the effectiveness, the SST k-ω model was selected for the simulation. SIMPLE coupling scheme and the second-order upwind algorithm were applied in the simulation. The convergence criteria were set at 10^{-5} for relative residuals, which required around 3000 iterations.

Fig. 9(b) compares the measured adiabatic effectiveness with the predicted numerical results for the 777-shaped holes at M=1.5. Note that, the recovery temperature mentioned in Eq. (2) is obtained by performing a numerical simulation without coolant injections. Generally, the simulated effectiveness results (pattern and film distributions) are consistent with the measured results, where less than 15% difference was observed between the measured and predicted results. The discrepancy could be originated from the isotropic assumptions of the turbulence models, leading to unexpected coolant diffusion. Therefore, the simulation provides acceptable results and will be then applied to obtain flow structures at the endwall region for both film cooling configurations.

3.5 Flow structures obtained from the numerical simulation

To uncover the endwall flow structures, simulations were conducted to explore the interactions between coolant film and the mainstream flow structures, and to reveal the underlying physics for improved effectiveness of BDSIC. In this study, the second invariant of the velocity gradient tensor, defined as the Q-criterion, is used to qualitatively show the vortex core region. The Q-criterion (i.e., see Eq. (5)) was applied to show the vortex structures, where Ω_{ij} and S_{ij} are the rotation and strain rates, respectively. Note that, a positive Q-isosurface was preferred [41] since it represents a true structure's rotation rather than its strain regardless of the vorticity direction.

$$Q = \frac{1}{2}\left(\Omega_{ij}\Omega_{ij} - S_{ij}S_{ij}\right) \tag{5}$$

$$\Omega_{ij} = \frac{1}{2}\left(\frac{\partial u_i}{\partial x_j} - \frac{\partial u_j}{\partial x_i}\right) \tag{6}$$

$$S_{ij} = \frac{1}{2}\left(\frac{\partial u_i}{\partial x_j} + \frac{\partial u_j}{\partial x_i}\right) \tag{7}$$

Fig. 10 shows the vortex core iso-surface above the endwall for various coolant film coverage (with Q-criterion sets to 2×10^7). The figures clearly show the existence of passage vortex (PV), horseshoe vortex (HV), and counter vortex (CV). A horseshoe vortex is generated due to the rolling up of the shear layer at the leading-edge of the blade. The PS leg of the HV extends

its way across the passage to the downstream, merging with the PV, while the SS leg of the HV stays at the junction of endwall near the SS, extending to become CV. The PV propagates from the PS to the SS, causing significant crossflow behavior on the endwall surface shown by the near-wall streamlines. This phenomenon matches with the deflection and accumulation of coolant film in the near SS region shown in Figs. 4 and 6. Carefully inspecting the position of PV, the BDSIC holes effectively compels the PV to attach to PS surface compared with the 777-shaped hole case, which can be observed from the vortex cores and streamlines. This explains the improvement of coolant film coverage at the endwall near the PS. Meanwhile, the strength of the SS leg of HV is observed to reduce in the BDSIC compared with the 777-shaped hole. The close-view near the SS shows the influences of the HV on the coolant distribution, observing attached coolant of the BDSIC compared with the 777-shaped holes. This indicates the reduced mixing of coolant and mainstream in this region, especially the BDSIC, which corresponds with the aforementioned elimination of hard-to-cool region at the leading-edge conjunction.

Streamwise vorticity (ω_x) distributions immediately downstream the 777-shaped holes and BDSIC holes at M=1.5 are presented in Fig. 11. Three different locations across the passage are illustrated for both configurations. As shown clearly in Fig. 11(a), the middle hole of baseline presents a pair of counter-rotating vortex (CRVP), which is the dominant vortex structure of jet-in-crossflow. However, due to the PV along the endwall, the 777-shaped holes close to the PS and SS will encounter mainstream flow equivalent to a compound angle cooling, where the incoming flow has a compound angle with the coolant jet. The leeward leg of the CRVP is strengthened and overlaps the windward leg for both hole locations mentioned above. The CRVP's red leg is enhanced for near-PS hole while its blue leg enlarged for near-SS hole. This is consistent with the archived results [42, 43]. Fig. 11(b) shows the streamwise vorticity downstream of the BDSIC holes. For the middle hole, the BDSIC induced a pair of strong anti-counter-rotating vortex (anti-CRVP, rotating opposite to CRVP), canceling the detrimental effect of CRVP and helps to suppress and laterally spread the coolant film downstream of the holes over the endwall surface. These phenomena match with the presented results shown in Zhou and Hu's work [28]. Similarly, the deflected flow caused by the complex flow structures introduces a compound angle for the holes near the PS and the SS. For these holes, it can observe that the windward leg of the anti-CRVP is strengthened and merges with the leeward leg of the CRVP, completely wrapping the windward leg of the CRVP. Due to its dune
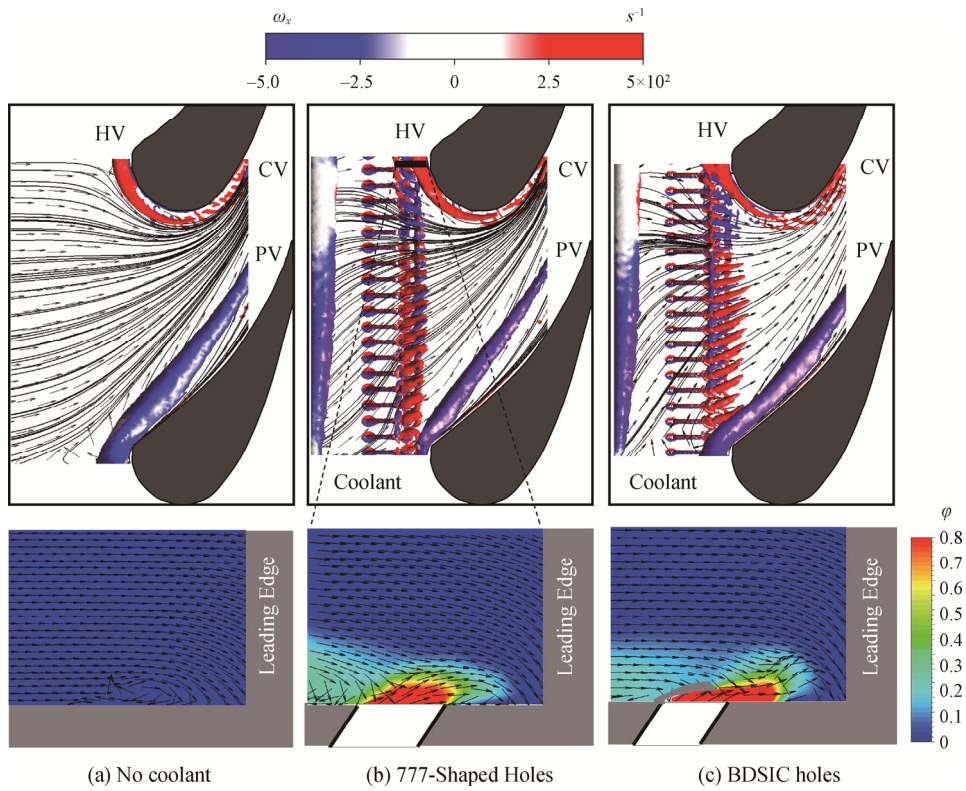
Fig. 10   Endwall vortex core iso-surfaces and near-wall streamlines at M=1.5
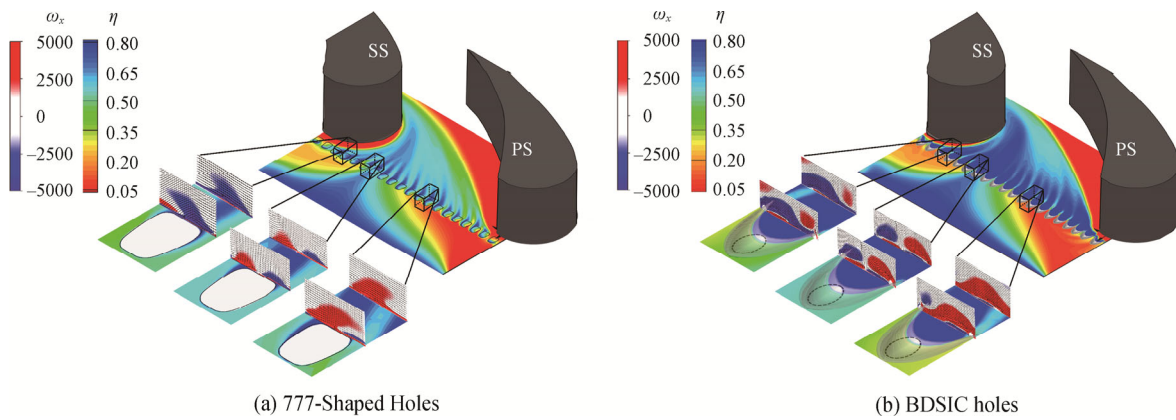
Fig. 11   Comparisons of streamwise vorticity distributions immediately downstream of (a) 777-Shaped Holes and (b) BDSIC holes at M=1.5

shape and compound angle, the coolant film of BDSIC is therefore spread wider and leads to improved effectiveness compared with the 777-shaped holes. Though the BDSIC exhibits promising results, the flow structure results raise our interest in studying the influence of compound angle on the effectiveness for further optimization of BDSIC endwall cooling performance in the future.

4. Conclusion

The present study compared the adiabatic film cooling effectiveness at the endwall region for the 777-shaped

hole and sand-dune inspired holes under various blowing ratios. Experimental measurements were conducted using PSP technique in a single-passage wind tunnel (Ma_{exit}= 0.84). The CO_2 was selected as coolant (DR=1.53), where it was separately discharged from the slot and coolant holes. The slot's blowing ratio was fixed at M=0.3 while the blowing ratio of the single row of holes ranges from M=0.5 to 2.0. In addition to effectiveness contours, lateral and area-averaged results were used to evaluate the overall performance of both configurations. Corresponding flow structures are further explored through numerical simulations. The major conclusions are:

(1) With the increase of blowing ratio, both configurations exhibited a significantly increased film cooling effectiveness. No significant take-off of coolant jet is observed for both holes when the blowing ratio increased from 0.5 to 2.0.

(2) The pressure gradient within passage forced the coolant stream to flow toward the endwall SS surface, rendering the highest cooling effectiveness near SS, following by the middle region, but relatively under-cooled for the near PS.

(3) The BDSIC holes outperform the 777-shaped holes at all blowing ratios. The most significant increase of effectiveness happens at the endwall region closer to the PS, showing 150% enhancement at M=0.5 and 26% at M=2.0 in regionally area-averaged effectiveness compared with the shaped hole.

(4) The increase is contributed to the three reasons: First, the hollowed BDSIC structure prevents coolant from penetrating to the mainstream, suppressing the coolant attach to the endwall surface. Second, the dune shape turns the coolant stream to discharge tangentially, and the increased momentum helps the coolant film to resist the deviation effect of passage vortex, thus better protect the surface. Finally, the anti-CRVP induced by the BDSIC structure counteracts the detrimental effect of CRVP, enhancing the spreading of coolant downstream.

Though the BDSIC shows great potential for endwall cooling applications, especially for the hard-to-cool regions such as the near-PS and leading-edge conjunction regions, the BDSIC's configurations (such as hole arrangements and compound angle effect), as well as the thermal heat flux across the dune, should be further evaluated due to the intensive heat transfer and flow interactions between the coolant film and passage flow. In general, the findings of this work are intended to improve the endwall cooling by using novel BDSIC, which can be fabricated with the turbine as an integral component when additive manufacturing for hot section components is feasible in the future.

Acknowledgements

References

[1]   Bogard D.G., Thole K.A., Gas turbine film cooling. Journal of Propulsion and Power, 2006, 22(2): 249–270.

[2]   Bunker R.S., A review of shaped hole turbine film-cooling technology. Journal of Heat Transfer, 2005, 127(4): 441–453.

[3]   Han J., Dutta S., Ekkad S., Gas turbine heat transfer and cooling technology, second ed., New York, 2012.

[4]   Du W., Luo L., Wang S., Zhang X., Effect of the dimple location and rotating number on the heat transfer and flow structure in a pin finned channel. International Journal of Heat and Mass Transfer, 2018. DOI: 10.1016/j.ijheatmasstransfer.2018.08.045.

[5]   Lei L., Wei D., Songtao W., Weilong W., Xinghong Z., Multi-objective optimization of the dimple/protrusion channel with pin fins for heat transfer enhancement. International Journal of Numerical Methods for Heat Fluid Flow, 2019, 29(2): 790–813.

[6]   Langston L.S., Crossflows in a turbine cascade passage. Journal of Engineering for Power, 1980, 102(4): 866-874.

[7]   Friedrichs S., Hodson H.P., Dawes W.N., Distribution of film-cooling effectiveness on a turbine endwall measured using the ammonia and diazo technique. Proceedings of the ASME 1995 International Gas Turbine and Aeroengine Congress and Exposition, 1995. DOI: 10.1115/95-GT-001.

[8]   Nicklas M., Film-cooled turbine endwall in a transonic flow field: Part II—heat transfer and film-cooling effectiveness. Journal of Turbomachinery, 2001, 123(4): 720–729.

[9]   Thole K.A., Knost D.G., Heat transfer and film-cooling for the endwall of a first stage turbine vane. International Journal of Heat and Mass Transfer, 2005, 48(26–27): 5255–5269.

[10]   Knost D.G., Thole K.A., Adiabatic effectiveness measurements of endwall film-cooling for a first-stage vane. Journal of Turbomachinery, 2005, 127(2): 297–305.

[11]   Shiau C.C., Chen A.F., Han J.C., Azad S., Lee C.P., Full-scale turbine vane endwall film-cooling effectiveness distribution using pressure-sensitive paint technique. Journal of Turbomachinery, 2018, 140(2): 021009. DOI: 10.1115/1.4032166.

[12]   Shiau C.C., Sahin I., Wang N., Han J.C., Xu H., Fox M., Turbine vane endwall film cooling comparison from five film-hole design patterns and three upstream injection angles. Proceedings of the ASME Turbo Expo 2018: Turbomachinery Technical Conference and Exposition. Volume 5C: Heat Transfer. Oslo, Norway. June 11–15, 2018. DOI: 10.1115/1.4042057.

[13]   Chowdhury N.H.K., Shiau C.-C., Han J.-C., Zhang L., Moon H.-K., Turbine vane endwall film cooling study from axial-row configuration with simulated upstream leakage flow. Proceedings of the ASME Turbo Expo 2017: Turbomachinery Technical Conference and Exposition, 2017. DOI: 10.1115/GT2017-63144.

[14]   Chowdhury N.H.K., Shiau C.-C., Han J.-C., Zhang L., Moon H.-K., Turbine vane endwall Film cooling with slashface leakage and discrete hole configuration. Journal

of Turbomachinery, 2017, 139(6): 061003.

[15] Müller G., Landfester C., Böhle M., Krewinkel R., Turbine vane endwall film cooling effectiveness of different purge slot configurations in a linear cascade. Journal of Turbomachinery, 2020, 142(3): 031008.

[16] Barigozzi G., Benzoni G., Franchini G., Perdichizzi A., Fan-shaped hole effects on the aero-thermal performance of a film-cooled endwall. Journal of Turbomachinery, 2006, 128(1): 43–52.

[17] Colban W., Thole K., Influence of hole shape on the performance of a turbine vane endwall film-cooling scheme. International Journal of Heat and Fluid Flow, 2007, 28(3): 341–356.

[18] Colban W., Thole K.A., Haendler M., A comparison of cylindrical and fan-shaped film-cooling holes on a vane endwall at low and high freestream turbulence levels. Journal of Turbomachinery, 2008, 130(3): 031007.

[19] Sundaram N., Thole K.A., Bump and trench modifications to film-cooling holes at the vane-endwall junction. Journal of Turbomachinery, 2008, 130(4): 041013.

[20] Sundaram N., Thole K.A., Film-cooling flowfields with trenched holes on an endwall. Journal of Turbomachinery, 2009, 131(4): 041007.

[21] Barigozzi G., Franchini G., Perdichizzi A., Ravelli S., Effects of trenched holes on film cooling of a contoured endwall nozzle vane. Journal of Turbomachinery, 2011, 134(4): 041009.

[22] Zhang G., Liu J., Sundén B., Xie G., Comparative study on the adiabatic film cooling performances with elliptical or super-elliptical holes of various length-to-width ratios. International Journal of Thermal Sciences, 2020, 153: 106360.

[23] Zhu R., Zhang G., Li S., Xie G., Combined-hole film cooling designs based on the construction of antikidney vortex structure: a review. Journal of Heat Transfer, 2020, 143(3): 030801.

[24] Choi D.-W., Lee K.-D., Kim K.-Y., Analysis and optimization of double-jet film-cooling holes. Journal Thermophysics and Heat Transfer, 2013, 27(2): 246–254.

[25] Zhang G., Liu J., Sundén B., Xie G., On the improvement of film cooling performance using tree-shaped network holes: A comparative study. Numerical Heat Transfer, Part A: Applications, 2018, 74(4): 1121–1138.

[26] Zhou W., Qenawy M., Shao H., Peng D., Wen X., Liu Y., Turbine vane endwall film cooling with barchan-dune shaped ramp in a single-passage transonic wind tunnel. International Journal of Heat and Mass Transfer, 2020, 162: 120350.

[27] Zhou W., Hu H., Improvements of film cooling effectiveness by using Barchan dune shaped ramps. International Journal of Heat and Mass Transfer, 2016,

103: 443–456.

[28] Zhou W., Hu H., A novel sand-dune-inspired design for improved film cooling performance. International Journal of Heat and Mass Transfer, 2017, 110: 908–920.

[29] Zhou W., Peng D., Liu Y., Hu H., Assessment of film cooling's surface quantities using pressure- and temperature-sensitive paint: Comparisons between shaped and sand-dune inspired holes. Experimental Thermal and Fluid Science, 2019, 101: 16–26.

[30] Buck F.A., Prakash C., Design and evaluation of a single passage test model to obtain turbine airfoil film cooling effectiveness data. Proceedings of the ASME 1995 International Gas Turbine and Aeroengine Congress and Exposition, 1995. DOI: 10.1115/95-GT-019.

[31] Kodzwa P.M., Eaton J.K., Film effectiveness measurements on the pressure surface of a transonic airfoil. Journal of Propulsion and Power, 2010, 26(4): 837–847.

[32] Kodzwa P.M.Jr., Vicharelli A., Medic G., Elkins C.J., Eaton J.K., Laskowski G.M., Durbin P.A., Evaluation of alternatives for two-dimensional linear cascade facilities. Journal of Turbomachinery, 2009, 131(3): 031001.

[33] Qenawy M., Yuan L., Liu Y., Peng D., Wen X., Zhou W., A novel single-passage transonic wind tunnel for turbine-vane film cooling. Journal of Engineering for Gas Turbines and Power, 2020, 142(7): 071009.

[34] Arts T., Lambertderouvroit M., Rutherford A.W., Aero-thermal investigation of a highly loaded transonic linear turbine guide vane cascade. Proceedings of the ASME 1990 International Gas Turbine and Aeroengine Congress and Exposition,1990. DOI: 10.1115/90-GT-358.

[35] Schroeder R., Thole K., Adiabatic effectiveness measurements for a baseline shaped film cooling hole. Proceedings of the ASME Turbo Expo 2014: Turbine Technical Conference and Exposition, 2014. DOI: 10.1115/GT2014-25992.

[36] Han J.-C., Rallabandi A., Turbine blade film cooling using PSP technique. Frontiers in Heat and Mass Transfer, 2010, 1: 013001.

[37] Wright L.M., Gao Z., Varvel T.A., Han J.C., Assessment of steady state PSP, TSP, and IR measurement techniques for flat plate film cooling. Proceedings of the ASME 2005 Summer Heat Transfer Conference collocated with the ASME 2005 Pacific Rim Technical Conference and Exhibition on Integration and Packaging of MEMS, NEMS, and Electronic Systems, 2005. DOI: 10.1115/HT2005-72363.

[38] Charbonnier D., Ott P., Jonsson M., Cottier F., Köbke T., Experimental and numerical study of the thermal performance of a film cooled turbine platform. Proceedings of the ASME Turbo Expo 2009: Power for Land, Sea, and Air, 2009. DOI: 10.1115/GT2009-60306.

[39] Johnson B., Hu H., Measurement uncertainty analysis in determining adiabatic film cooling effectiveness by using pressure sensitive paint technique. Journal of Turbomachinery, 2016, 138(12): 121004.

[40] Shih T.H., Liou W.W., Shabbir A., Yang Z., Zhu J., A new *k-ε* eddy viscosity model for high reynolds number turbulent flows. Computers and Fluids, 1995, 24(3): 227–238.

[41] Dubief Y., Delcayre F., On coherent-vortex identification

in turbulence. Journal of Turbulence, 2000, 1: N11. DOI: 10.1088/1468-5248/1/1/011.

[42] Haydt S., Lynch S., Cooling effectiveness for a shaped film cooling hole at a range of compound angles. Journal of Turbomachinery, 2019, 141(4): 041005.

[43] Li Y., Zhang Y., Su X., Yuan X., Experimental and numerical investigations of shaped hole film cooling with the influence of endwall cross flow. International Journal of Heat and Mass Transfer, 2018, 120: 42–55.